Slow-light effect in dual-periodic photonic lattice

Alexey G. Yamilov,[1,*] Mark R. Herrera,[1] and Massimo F. Bertino[2]

[1]*Department of Physics, Missouri University of Science and Technology, Rolla, Missouri 65409, USA*
[2]*Department of Physics, Virginia Commonwealth University, Richmond, Virginia 23824, USA*
*Corresponding author: yamilov@mst.edu

We present analytical and numerical studies of a photonic lattice with short- and long-range harmonic modulations of the refractive index. Such structures can be prepared experimentally with holographic photolithography. In the spectral region of the photonic bandgap of the underlying single-periodic crystal, we observe a series of bands with anomalously small dispersion. The related slow-light effect is attributed to the long-range modulation of the photonic lattice that leads to formation of an array of evanescently coupled high-Q cavities. The band structure of the lattice is studied with several techniques: (i) transfer matrix approach; (ii) an analysis of resonant coupling in the process of band folding; (iii) effective-medium approach based on coupled-mode theory; and (iv) the Bogolyubov–Mitropolsky approach. The latter method, commonly used in the studies of nonlinear oscillators, was employed to investigate the behavior of eigenfunction envelopes and the band structure of the dual-periodic photonic lattice. We show that reliable results can be obtained even in the case of large refractive index modulation. © 2008 Optical Society of America

OCIS codes: 230.4555, 230.5298, 350.5500.

1. INTRODUCTION

Optical pulse propagation in dielectrics is determined by the group velocity $v_g = d\omega(K)/dK$, where the dispersion $\omega(K)$ relates the frequency ω and the wave-vector K inside the medium. One of the appealing features of photonic crystals has become the possibility to alter the dispersion of electromagnetic waves [1] so that in a certain spectral region v_g becomes significantly smaller than the speed of light in vacuum. This "slow-light" effect [2] attracted a great deal of practical interest because it can lead to low-threshold lasing [3–5], pulse delay [6,7], optical memories [8], and enhanced nonlinear interactions [9–11]. Several approaches to obtaining low dispersion in photonic crystal structures have been exploited.

(i) At frequencies close to the photonic band edge, $\omega(K)$ becomes flat and group velocity approaches zero due to the Bragg effect at the Brillouin zone boundary. This property has been extensively studied and used in practice to control the spontaneous emission [12] and gain enhancement in lasers [3–5]. However, a large second-order dispersion (i.e., dependence of v_g on frequency) in the vicinity of the band edge leads to strong distortions in a pulsed signal that makes this approach unsuitable for, e.g., information processing applications.

(ii) High-order bands in two- and three-dimensional photonic crystals can have small dispersion not only at the Brillouin zone boundary but also throughout the band [13,14] where the second-order dispersion can be significantly reduced. Nevertheless, these high-frequency photonic bands allow little control over v_g and are not spectrally isolated from other bands. These drawbacks and the increased sensitivity to fabrication errors [15] limit the practical value of this approach.

(iii) Based on the coupled resonator optical waveguide (CROW) [8,16–18] idea, a low-dispersion photonic band can be purposefully created via hybridization of high-Q resonances arising from periodically positioned structural defects [19–21]. This *spectrally isolated* defect band is formed inside the photonic bandgap, with a dispersion relation given by

$$\omega(K) = \Omega[1 + \kappa \cos(KL)]. \quad (1)$$

Here Ω is the resonance frequency for a single defect, κ is the coupling constant (assumed to be small), and L is the spacing between defects. These adjustable parameters allow one to control dispersion in the band, and hence v_g, without significant detrimental effects due to second-order dispersion.

A periodic arrangement of structural defects in the photonic crystal, described in (iii), creates a *photonic supercrystal* (PhSC) with short-range quasi-periodicity on the scale of the lattice constant and long-range periodicity on the defect separation scale [22–29]. We have recently proposed a PhSC with dual-*harmonic* modulation of the refractive index [30] [see Eq. (2)] that can be fabricated [31,32] via a single-step interference photolithography technique. Because all resonators are produced at once, our design minimizes fabrication error margin and ensures the large-scale periodicity essential for hybridization of the resonances of individual cavities in an experiment.

The purpose of this work is to theoretically investigate the optical properties of a one-dimensional PhSC using a combination of analytical and numerical techniques. We consider the dielectric function that can be produced with the interference photolithography method

$$\varepsilon(x) = \varepsilon_0 + \frac{\Delta\varepsilon/2}{1+\gamma}[1 + \gamma\cos(2\pi x/L)][1 + \cos(2\pi x/a)]. \quad (2)$$

Here ε_0 is the background dielectric constant. The amplitude of the short-range (on scale a) modulation gradually changes from $\Delta\varepsilon[(1-\gamma)/(1+\gamma)]$ to $\Delta\varepsilon$. $L=Na$ sets the scale of the long-range modulation; $N \gg 1$ is an integer.

Each of the four theoretical techniques used in this work has its strengths and its weaknesses. The numerical transfer-matrix approach, employed in Section 3, can deal with any modulation of the refractive index. Unlike the other methods, it also allows us to study the transmission spectra of *finite* segments of the PhSC. One of the important conclusions obtained in Section 3 is the possibility of scale separation in the eigenstates of a PhSC with a large modulation of the refractive index (large $\Delta\varepsilon$). Inability to obtain an analytical description of the spectrum of the eigenstates or their spatial profiles is a limitation of this method.

With the help of the resonant approximation considered in Section 4, we analytically obtain the spectral position and the width of photonic bandgaps separating the flat bands under consideration. This information gives important physical insight into how the resonantly increased band-to-band interaction (repulsion) leads to a reduction of band dispersion. The applicability condition [see Eq. (14)] for this approach does not allow us to extend the treatment to the experimentally relevant case of large N and appreciable $\Delta\varepsilon$.

In Section 5 we apply the effective-medium approximation of [26] to our proposed dual-periodic crystals with large N. This method is related to the coupled-mode theory (CMT) [33] and treats the $\Delta\varepsilon$ term in Eq. (2) as a perturbation. In our case of large $\Delta\varepsilon$, the effective-medium approximation accurately describes the eigenstates of the PhSC on a *qualitative* level. The quantization condition, Eq. (20), gives intuitive results for the spectrum.

In Section 6, similar to the previous approach, we transform the Maxwell equations to amplitude and phase form. Then, without making the assumption $\Delta\varepsilon \ll 1$, we apply the scale separation technique of Bogolyubov–Mitropolsky to obtain a system of nonlinear differential equations for the amplitude and the phase of eigenfunctions. The spectrum of the system can be found numerically by requiring periodicity of the eigenfunction. We show that this method agrees *quantitatively* with direct simulations by the transfer-matrix approach of Section 3. Section 7 concludes our study with a summary of the results obtained within the above approaches.

2. EXPERIMENTAL REALIZATIONS OF A PhSC

In our previous work [30] we proposed employment of holographic photolithography to fabricate a modulated photonic crystal, or PhSC. The experimental quantum dot ultraviolet photolithography (QDPL) technique—a bottom-up technique that allows synthesis of quantum dots and other nanoparticles in selected regions of porous matrices [31,32]—is suitable for this purpose. The change of the dielectric function in such systems is related to the

local density of quantum dots, which is proportional to the local intensity of the electromagnetic wave used when exposing the sample. Manipulation of the four lithographic beams allows for easy control over the structural properties of the resultant systems, as described in [30]. Such a PhSC has dual-harmonic modulations, short and long range, similar to that described by Eq. (2). The latter functional form was chosen to enable an analytic treatment and differs slightly from the expression in [30]. Nonetheless, it shows the same spectral composition and modulation property. The discrepancy between the two forms is expected to cause only small deviations from the analytical results obtained in this work. Furthermore, the differences become insignificant in the limit $N \gg 1$.

Our estimates show that structures operating at $\lambda \sim 800$ nm would require $a \sim 400$ nm and $L = Na \sim 20$ μm. As it has been demonstrated in [18], already a dozen resonators can be employed as a functional delay line. With the holographic photolithography technique, it should be fairly straightforward to create hundreds of PhSC cavities (of size L).

Dual-periodic harmonic modulation of the refractive index can also be experimentally realized in optically induced photorefractive crystals [34–36]. Although, the index contrast obtained is several orders of magnitude less than with QDPL [31,32], the superlattices created in photorefractive materials offer the possibility of dynamical control—a feature lacking in the quantum dot system. While the study of dynamical and nonlinear phenomena in dual-periodic lattices is of significant interest, it goes beyond the scope of the present publication and will not be considered in this work.

3. TRANSFER MATRIX ANALYSIS

The transmission–reflection spectrum of a one-dimensional PhSC of finite length, and the band structure of its infinite counterpart, can be obtained numerically via the transfer-matrix approach. Propagation of a field with wave vector $k = \omega/c$ through an infinitesimal segment of length dx is described by the transfer matrix [37]

$$\hat{M}(x, x+dx) = \begin{bmatrix} \cos(kn(x)dx) & n^{-1}(x)\sin(kn(x)dx) \\ -n(x)\sin(kn(x)dx) & \cos(kn(x)dx) \end{bmatrix},$$
$$(3)$$

where we have assumed that the refractive index $n(x)$ does not change appreciably over that distance. The matrix $\hat{M}(x, x+dx)$ relates the electric field and its spatial derivative $\{E, (1/k)(dE/dx)\}$ at $x+dx$ and x. The total transfer matrix of a finite system is then given by the product of individual matrices

$$\hat{M}_{\text{tot}} = \prod_{x=0}^{L} \hat{M}(x, x+dx). \quad (4)$$

Since in our case the refractive index $n(x) = \varepsilon^{1/2}(x)$, Fig. 1(a), is not a piecewise constant (in contrast to [26,27]) but a continuous function of coordinate, one has to resort to numerical simulations. In what follows we apply either scattering or periodic boundary conditions to obtain the
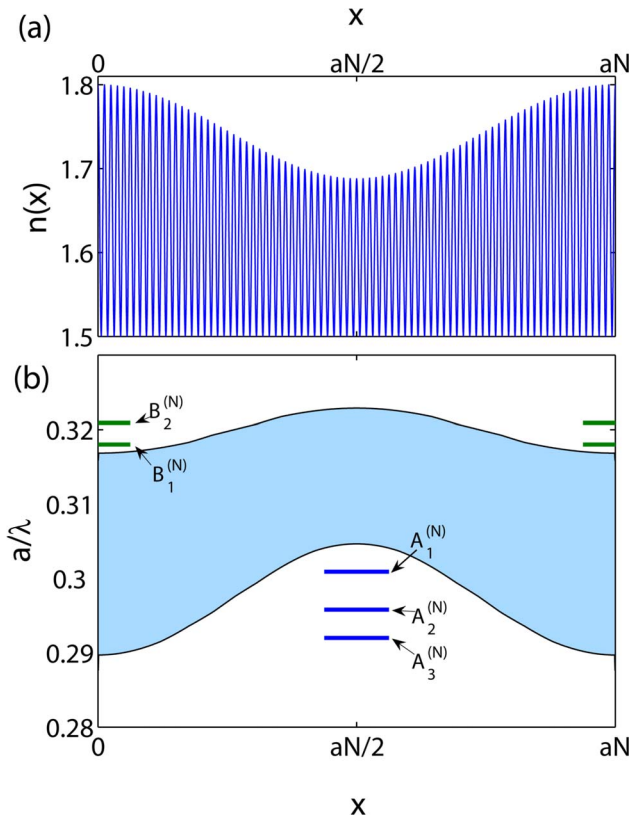
Fig. 1.   (Color online) (a) Dependence of the index of refraction in a dual-periodic photonic crystal as defined by Eq. (2). We used $\varepsilon_0 = 2.25$, $\Delta\varepsilon = 1$, $N = 80$, and the modulation parameter γ is equal to 0.25. (b) Local (position-dependent) photonic bandgap diagram for $n(x)$ in (a). $A_i^{(N)}$ and $B_i^{(N)}$ mark the frequencies of the foremost photonic bands on the long- and short-wavelength sides of the photonic bandgap of the corresponding single-periodic crystal.

Fig. 2.   (Color online) (a) Transmission coefficient through a finite segment of length L (one period) of the periodic superstructure defined in Fig. 1. Solid and dashed curves correspond to $0 < x < Na$ and $-Na/2 < x < Na/2$ segments [shown in the inset of panel (b)], respectively. (b) Solid and dashed thin curves plot the corresponding phase of $t(\omega)$. Bold line depicts the Bloch number $K(\omega) \times a$ of the infinite crystal computed using Eq. (5).

transmission coefficient and Bloch number $K(\omega)$, respectively.

Figure 2(a) plots the transmission coefficient through one period of the dual-periodic system shown in Fig. 1. A series of progressively sharper resonances occur on the lower or upper edge of the spectral gap of the underlying single-periodic structure. Whether the peaks occur at the lower or upper band edge depends on the particular definition of the unit cell, as shown in the inset of Fig. 2(a). One can obtain insight into this effect by examining the modulation of the spectral position of the "local" photonic bandgap (PBG) with the position as shown in Fig. 1(b). This analysis is meaningful on a length scale of the order of $a \ll \Delta x \ll L \equiv Na$. This condition can be satisfied in our case of slow modulation with large N. At frequencies such as $A_i^{(N)}$ in Fig. 1(b), wave propagation is allowed in the vicinity of $x = aN(1/2 + m)$, whereas at the regions $x = aN(m)$ it is locally forbidden, m being an integer. When considering a segment of the lattice with $0 < x < Na$, resonant tunneling via electromagnetic states $A_i^{(N)}$ of the cavity at the geometrical center leads to low-frequency peaks in the transmission coefficient, indicated by the solid curve in Fig. 2(a). On the other hand, transmission through the segment $-Na/2 < x < Na/2$ exhibits a series of sharp resonances. These correspond to tunneling via $B_i^{(N)}$ cavity states in the high-frequency region.
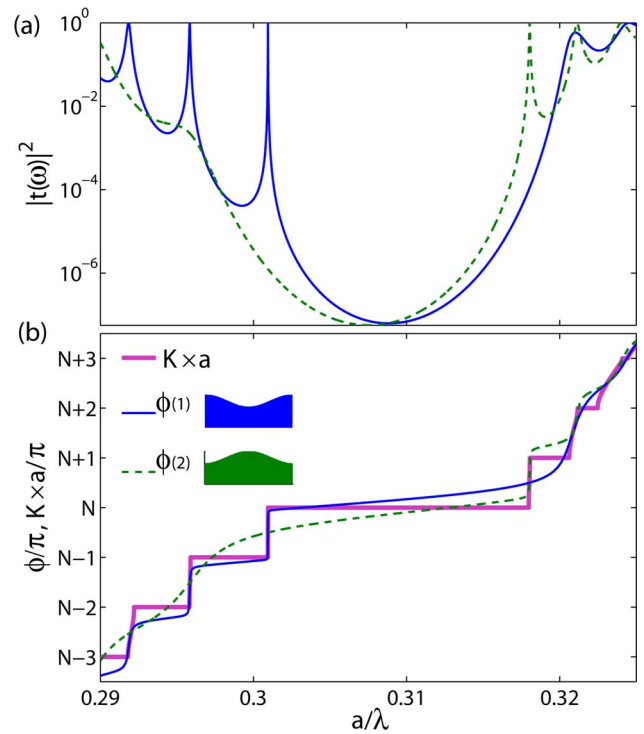
The transmission coefficient through a finite segment of length L (equal to one period) can be related to the band structure of the corresponding periodic lattice [27] as

$$\cos(K(\omega)L) = \mathrm{Re}\left[\frac{1}{t(\omega)}\right] \equiv \frac{1}{|t(\omega)|}\cos(\phi(\omega)), \qquad (5)$$

where we have introduced the phase of the transmission coefficient $\phi(\omega)$ through $t = |t|\exp[i\phi]$. Figure 3 shows that hybridization of the cavity resonances considered above leads to the formation of flat photonic bands. Their low dispersion and small group velocity may be exploited [30] for practical applications.

In the vicinity of an isolated transmission resonance, $t(\omega)$ is given by the Lorentzian

$$t(\omega) = \frac{(-1)^N(\Gamma/2)}{i(\Gamma/2) - (\omega - \omega_0)}, \qquad (6)$$

where Γ is the full width at half-maximum (FWHM) of the resonance and ω_0 is the resonant frequency. Substitution of Eq. (6) into Eq. (5) gives the flat band described by

$$\omega(K) = \omega_0[1 \pm \kappa\cos(KL)], \qquad (7)$$

where $\kappa = \Gamma/2\omega_0 = 1/Q \ll 1$, and Q is the cavity Q factor. Thus, the decrease of group velocity in the PhSC is directly related to the increase of confinement and the decrease of coupling between neighboring cavities. In our PhSC both these factors are described by the same
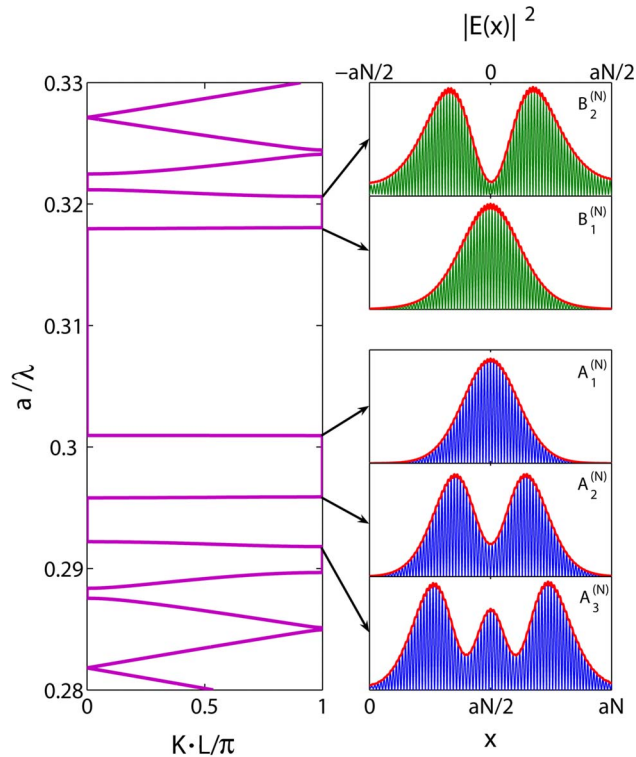
Fig. 3.   (Color online) Left panel shows dispersion of a PhSC $\omega(K)$ reduced to the first Brillouin zone. The eigenmodes that correspond to the series of flat bands in the vicinity of the parent bandgap of the single periodic crystal are depicted on the right. Calculations were performed for the structure described in Fig. 1.

parameter—the cavity Q factor. In a single-periodic photonic crystal of finite length, the Q factor of a band-edge mode depends on the system size. Comparing Figs. 1(b) and 3, one can see that $A_i^{(N)}, B_i^{(N)}$ modes are in fact band-edge modes in their intervals of free propagation. In our case L gives the characteristic length and, as we demonstrate below, also determines the mode frequency. As N increases, the eigenfrequencies of the modes shift towards the bandgap. The associated decrease of the local group velocity contributes to an increase of the Q factor of the resonators and to a further reduction of the group velocity in $A_i^{(N)}, B_i^{(N)}$ bands in the $N \rightarrow \infty$ limit.

Equation (5) suggests that the dispersion relation $\omega(K)$ is independent of how the segment of length L (the period of our structure) is chosen. However, the transmission coefficient through the $0 < x < Na$ and $-Na/2 < x < Na/2$ segments of the crystal shows very different spectral composition [Fig. 2(a)]. To understand how these markedly different functions lead the same $\omega(K)$, we will analyze the phase of the transmission coefficient ϕ, shown in Fig. 2(b).

In a one-dimensional periodic system such as ours, the wavenumber $K(\omega)$ in Eq. (5) is equal to the integrated density of electromagnetic states. It is by definition a monotonically increasing function of frequency in the extended Brillouin zone scheme. In PhSC, KL increases by π every time the frequency is increased through an allowed band; *cf.* bold curve in Fig. 2(b). At the frequency in the middle of the band, $\cos(KL) = 0$ because $KL = \pi(m$

$+1/2)$. From Eq. (5) one can see that ϕ should be equal to $\pi(m+1/2)$ at the same frequency. In the finite system, the mode counting phase $\tilde{\phi}$ defined [38] as $\tan(\tilde{\phi}) = E'/E$ coincides with the phase of the transmission coefficient $\phi \equiv \tilde{\phi}$. This explains the monotonic behavior of $\phi(\omega)$. Equation (5) leads to the fact that quasi-states of the finite system occur at the same place as the corresponding band center of the lattice, irrespective of the definition of the unit cell. Thus, as can also be seen from Fig. 2(b), $\phi(\omega)$ and $K(\omega)L$ intersect at $\pi(m+1/2)$.

Taylor expansion of the phase around the frequency ω_0 at the center of a passband, where $K(\omega)L = \pi(m+1/2)$ gives

$$\cos(K(\omega)L) = (\omega - \omega_0) \frac{(-1)^m}{|t(\omega_0)|} \frac{\mathrm{d}\phi(\omega_0)}{\mathrm{d}\omega}. \qquad (8)$$

Here, the term that contained $\mathrm{d}|t(\omega_0)|/\mathrm{d}\omega$ dropped out because $\cos(K(\omega_0)L) = 0$. Comparing Eqs. (7) and (8) shows that it is $|t(\omega_0)|^{-1}\mathrm{d}\phi(\omega_0)/\mathrm{d}\omega$ that determines $Q = 1/\kappa$ and not just $|t(\omega_0)|$. Suppressed transmission compensates for a slow phase change [e.g., solid curve in Fig. 2(b) in the high-frequency spectral region] and leads to an identical $K(\omega)$ for two different definitions of the unit cell.

We also note that if the segment is chosen such that the corresponding "cavity" is located in the geometrical center ($|t(\omega_0)| = 1$), the FWHM of the resonance (Γ) in the transmission coefficient is equal to the width of the passband in the periodic lattice. This fact follows from Eqs. (5) and (6). It further emphasizes the analogy with CROW structures that we explored in [30].

We conclude this section by noting that long-range refractive index modulation creates alternating spatial regions that can serve as resonators separated by the tunneling barriers. Hybridization of the cavity resonances creates a series of photonic bands with low dispersion. The envelope of the eigenstates in these bands $A_i^{(N)}, B_i^{(N)}$ is a slowly varying function of the coordinate (see Fig. 3). This effect stems from states proximity to the photonic band edge of the underlying single-periodic lattice. The possibility of a separation into short (a of rapid field oscillations) and long (L of the slow amplitude variation) length scales will further inform analytical studies presented in Sections 5 and 6.

4. RESONANT APPROXIMATION

Forbidden gaps in the spectra of a periodic system arise due to a resonant interaction of the wave with its Bragg-scattered counterpart [39]. The scattered wave appears due to the presence of Fourier harmonics in the spectrum of the periodic "potential," which in the case of the Helmholtz equation

$$E''(x) + \frac{\omega^2}{c^2}\delta\varepsilon(x)E(x) = \frac{\omega^2}{c^2}\bar{\varepsilon}E(x), \qquad (9)$$

is represented by $(\omega^2/c^2)\delta\varepsilon(x) \equiv (\omega^2/c^2)[\varepsilon(x) - \bar{\varepsilon}]$. Here we have introduced the average value of the dielectric function $\bar{\varepsilon} = \overline{\varepsilon(x)} = \varepsilon_0 + \Delta\varepsilon/[2(1+\gamma)]$. When $\gamma = 0$, the condition $\Delta\varepsilon/\bar{\varepsilon} \ll 1$ is sufficient to obtain the position and width of spectral gaps. Otherwise, an additional condition

$N(\Delta\varepsilon/\bar{\varepsilon})\ll 1$ needs to be satisfied instead. We will discuss the physical meaning of this condition at the end of this section.

We begin by noticing that $\delta\varepsilon(x)$ of our choice [Eq. (2)] contains only eight nonzero Fourier harmonics:

$$\varepsilon(x) = \sum_{m=-\infty}^{\infty} \varepsilon_m \exp\left[i\frac{2\pi}{L}mx \right], \qquad (10)$$

where $m=\{\pm 1, \pm(N-1), \pm N, \pm(N+1)\}$. This fact allows for an exhaustive study of all resonant interactions as follows. Expressing $E(x)$ in terms of its Fourier components

$$E(x) = \exp[iK(\omega)x] \sum_{m=-\infty}^{\infty} E_m \exp\left[i\frac{2\pi}{L}mx \right], \qquad (11)$$

leads to an infinite system of coupled linear equations

$$\left[\frac{\omega^2}{c^2}\bar{\varepsilon} - \left(K(\omega) + \frac{2\pi}{L}m \right)^2 \right]E_m + \frac{\omega^2}{c^2}\sum_{m'\neq 0} \varepsilon_{m'}E_{m-m'} = 0, \qquad (12)$$

where K is the Bloch number that varies in the first Brillouin zone $[0, \pi/L]$. For the extreme values of K there exists a spectral range where the term in brackets in Eq. (12) can become simultaneously small for certain values of m and $-m$ at $K=0$, and for m and $-m-1$ at $K=\pi/L$. If $\varepsilon(x)$ contains a harmonic $\varepsilon_{m'}$ such that it couples these two Fourier components, the overall infinite system [Eq. (12)] can be reduced to two resonant equations.

The results of such an analysis are summarized in Table 1 and the corresponding band structure is shown in Fig. 4. Introduction of the long-range modulation in the dielectric constant results in an expansion of the unit cell from a to $L=Na$ and, thus, to a reduction of the Brillouin zone, accompanied by the folding of photonic bands. The cases of even $N=2s$ and odd $N=2s+1$ should be distinguished. In the former, the primary photonic bandgap (II_e) of the single-periodic lattice reappears at $K=0$, whereas in the latter (II_o) it is located at $K=\pi/L$. Our analysis shows that the nearest frequency gaps, $\text{I}_{o,e}$ and $\text{III}_{o,e}$, also become resonant (Fig. 4). For the refractive index modulation of Eq. (2), the normalized width $\varepsilon_{(N-1)}/\bar{\varepsilon}$

Table 1. Results of Resonant Approximation Analysis of Eq. (12) With Dielectric Function Given by Eq. (2)[a]

Resonant K			
(Even N)	π/L	0	π/L
(Odd N)	0	π/L	0
Coupled components	$E_{-s}, E_{N-(s+1)}$	E_{s-N}, E_s	$E_{-(s+1)}, E_{N-s}$
Coupling harmonics	$\varepsilon_{-(N-1)}, \varepsilon_{N-1}$	$\varepsilon_{-N}, \varepsilon_N$	$\varepsilon_{-(N+1)}, \varepsilon_{N+1}$
Center frequency, ω_0	$\dfrac{c\pi}{\sqrt{\bar{\varepsilon}}L}(N-1)$	$\dfrac{c\pi}{\sqrt{\bar{\varepsilon}}L}N$	$\dfrac{c\pi}{\sqrt{\bar{\varepsilon}}L}(N+1)$
Normalized width, $\Delta\omega/\omega_0$	$\varepsilon_{(N-1)}/\bar{\varepsilon}$	$\varepsilon_N/\bar{\varepsilon}$	$\varepsilon_{(N+1)}/\bar{\varepsilon}$

[a]Three columns correspond to the three resonant photonic bandgaps that appear in the spectrum of the dual-periodic PhSC. The expressions hold for both even and odd N for the choice of parameter s: $N=2s$ and $N=2s+1$, respectively.
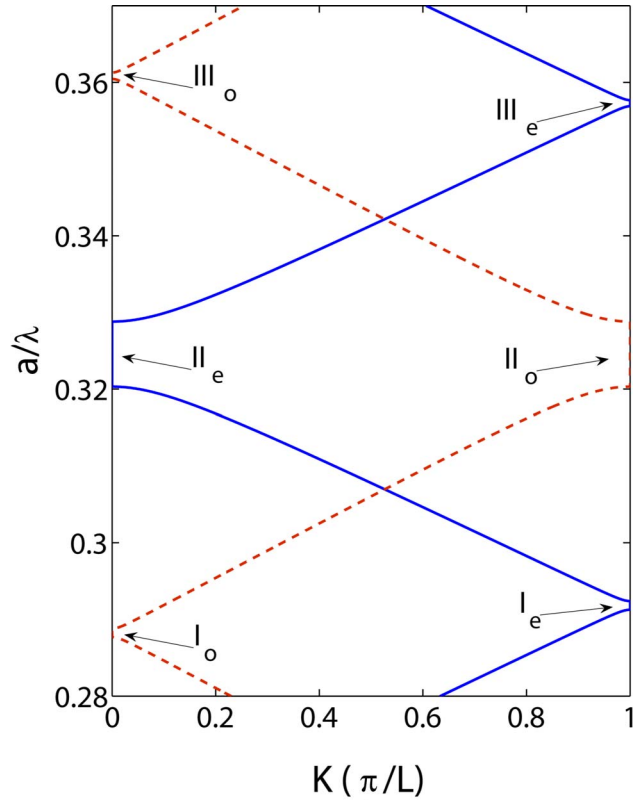

Fig. 4. (Color online) Dispersion relation computed with the transfer matrix formalism for $\varepsilon_0=2.25$, $\Delta\varepsilon=0.32$, $N=9$ (dashed curve), and $N=10$ (solid curve). The modulation parameter γ is equal to 0.25. For this set of parameters, the applicability condition [Eq. (13)] of the resonant approximation is satisfied.

$=(\gamma\Delta\varepsilon/4\bar{\varepsilon})/(1+\gamma)$ of the satellite gaps is smaller than that of the central gap by a factor of γ. By definition, this parameter is less than unity.

We can see that folding and the onset of the formation of flat $A_1^{(N)}$, $B_1^{(N)}$ bands is captured in this approximation. The criterion of its applicability can be found by considering the contributions of nonresonant terms in Eq. (12). We find that for all three gaps the criteria are qualitatively the same. Therefore, we present the detailed analysis of only one particular resonance, III_e. The condition that the closest nonresonant Fourier components E_{-s-2}, E_{-s}, E_{s-1}, and E_{s+1} be smaller than the resonant ones E_{-s-1} and E_s leads to the relation

$$\frac{(N+1)^2(\varepsilon_1 + \varepsilon_N)}{4N\bar{\varepsilon} + 2(N+1)^2\varepsilon_{N-1}} \ll 1. \qquad (13)$$

In the limit of very large N the second term in the denominator becomes dominant and this condition cannot be satisfied for any value of $\Delta\varepsilon$. Thus, N should be finite. The condition that the first term in the denominator be dominant is consistent with the entire inequality, Eq. (13), and is equivalent to $N\varepsilon_i/\bar{\varepsilon}\ll 1$. Taking the most restrictive case for ε_i we finally obtain

$$\frac{\Delta\varepsilon}{8\bar{\varepsilon}}N \ll 1, \qquad (14)$$

where we have neglected γ for simplicity.

Equation (14) has a clear physical meaning. Indeed, from Table 1, it is clear that the frequency of bandgaps I and III approach the central gap inherited from the single-periodic system as $1/N$. At some point a bandgap of width $\Delta\omega/\omega_0 = \varepsilon_i/\bar{\varepsilon}$ begins to substantially perturb the passband of width $K_{\max}c \simeq \omega_0/N$ separating consecutive gaps. The resonant approximation breaks when these two scales become comparable. This condition results in Eq. (14). In other words, the approximation considered in this section can at most capture the onset of the flattening trend in the $A_1^{(N)}$, $B_1^{(N)}$ bands and fails when N is increased to the point where these states become abnormally flat, i.e., where $\Delta\omega/K_{\max} \ll c/\bar{\varepsilon}$ throughout the band. More sophisticated approaches are considered in Sections 5 and 6.

5. EFFECTIVE-MEDIUM APPROXIMATION

Gratings written in the core of photosensitive optical fibers are often analyzed with the help of CMT [33]. In both shallow gratings with long-range modulation in fibers [26,28] and in our PhSC, the forward and backward (locally) propagating waves continuously scatter into each other. The advantage of CMT is that it considers the amplitudes of the forward and backward waves directly. This tremendously simplifies Maxwell equations. Reference [40] also considered fiber gratings with a deep piecewise constant index modulation. In this section we employ the CMT-based method developed by Sipe *et al.* [26] to obtain the spectral positions of the flat photonic bands formed in a PhSC.

For *shallow modulation*, i.e., small $\Delta\varepsilon$, our Eq. (2) can be brought to resemble the model function considered in [26]

$$n(x)/n_0 = 1 + \sigma(x) + 2\kappa(x)\cos[2k_0x + \varphi(x)], \quad (15)$$

with the following choice of parameters:

$$\sigma(x) = \frac{\dfrac{\gamma\Delta\varepsilon/4}{1+\gamma}}{\varepsilon_0 + \dfrac{\Delta\varepsilon/2}{1+\gamma}}\cos\frac{2\pi}{L}x,$$

$$\kappa(x) = \frac{\dfrac{\Delta\varepsilon/8}{1+\gamma}}{\varepsilon_0 + \dfrac{\Delta\varepsilon/2}{1+\gamma}}\left(1 + \gamma\cos\frac{2\pi}{L}x\right),$$

$$\varphi(x) \equiv 0, \quad n_0 = \left(\varepsilon_0 + \frac{\Delta\varepsilon/2}{1+\gamma}\right)^{1/2}, \quad k_0 = \pi/a. \quad (16)$$

The CMT of [26] is applicable as long as these functions have *a slow dependence on x*, a scale much larger than k_0^{-1}. This condition is indeed satisfied in the PhSC with $N \gg 1$.

By introducing a small detuning parameter

$$\delta = \frac{\omega - \omega_0}{\omega_0} \ll 1, \quad \omega_0 = \frac{k_0c}{n_0}, \quad (17)$$

we can, following [26], obtain the governing equation for the quantity E_{eff} related to the envelope of the electric field

$$\frac{d^2E_{\text{eff}}}{dx^2} + k_0^2n_{\text{eff}}^2(x,\omega)E_{\text{eff}} = 0. \quad (18)$$

Frequency and position dependent effective refractive index

$$n_{\text{eff}} = \{(\sigma(x) + \Delta)^2 - \kappa(x)^2\}^{1/2}, \quad (19)$$

determines whether propagation is locally allowed (real n_{eff}) or forbidden (imaginary n_{eff}). This is similar to our definition of the local PBG diagram, which we studied numerically in Section 3. Figure 5(b) compares CMT's region of evanescent propagation (solid curves) to the numerical calculation (dashed curves). We attribute the relatively small discrepancy observed there to the assumption of shallow modulation made in arriving at Eq. (19).

Equation (18) is formally similar to the Schrödinger equation. Our analysis in Section 3 shows that the single-period states associated with photonic bands $A_i^{(N)}, B_i^{(N)}$ are confined to the region of classically allowed propagation, in the language of quantum mechanics. By analogy, the Wentzel–Kramers–Brillouin (WKB) approximation of quantum mechanics can be applied [26] to determine the quantization of energies inside our optical equivalent of a quantum well
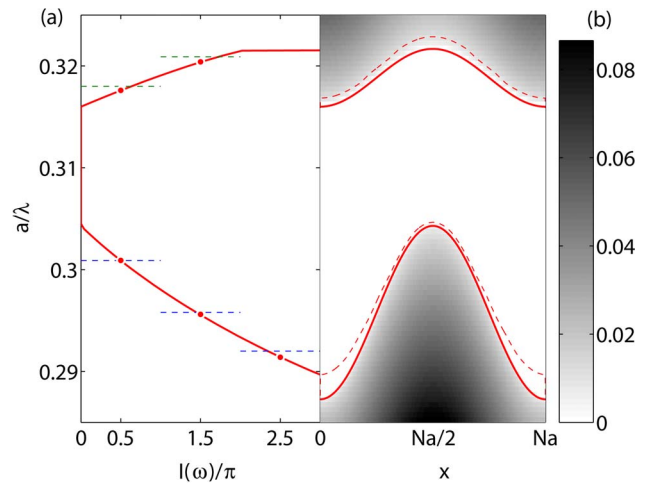

Fig. 5. (Color online) (a) Value of the integral in Eq. (20) (solid curve), as a function of frequency is shown. For easy comparison with (b), the plot is transposed so that ω is plotted along the y axis. The circles depict frequencies that satisfy the quantization condition of Eq. (20). The dashed lines denote the actual position of photonic states, as determined by direct numerical analysis of Section 3. (b) Gray-scale plot of $\text{Re}[n_{\text{eff}}(x,\omega)]$ given by Eq. (19). The solid curve shows the boundary of the region where $\text{Im}[n_{\text{eff}}(x,\omega)] \neq 0$. For comparison we also show the local PBG of Fig. 1(b) (dashed curve). In both (a) and (b), the parameters of Fig. 1 are adopted.

$$I(\omega) = k_0 \int_{x_L}^{x_R} n_{\text{eff}}(x,\omega)\mathrm{d}x = (m + 1/2)\pi, \qquad (20)$$

in which x_L and x_R are, respectively, the left and right turning points defined by the condition $n_{\text{eff}}(x_{L,R},\omega)=0$ and m is an integer. The solid curve in Fig. 5(a) depicts the value of the integral in Eq. (20), as a function of ω, obtained numerically. The filled circles denote the frequencies at which the quantization condition [Eq. (20)] is satisfied. In a system with the parameters we used for illustration in previous sections, the obtained solutions are in fair agreement with numerical results obtained with the transfer-matrix approach described in Section 3. This suggests that the index variation given by $\Delta\varepsilon = 1$, $\varepsilon_0 = 2.25$ was sufficiently small for this approach to still be qualitatively applicable.

We finish the current section by noting that it would be desirable to retain the attractive property of the CMT envelope approach without being constrained by the condition of small refractive index modulation. The latter may not always be justified in the experimental situation of interest [31,32]. In Section 6 we develop such an approach.

6. BOGOLYUBOV–MITROPOLSKY APPROACH

In this section we will consider the standing-wave solutions of Eq. (9). In this case, the corresponding $E(x)$ can be chosen to be a real function by an appropriate choice of normalization. Then, we make the Bogolyubov ansatz [41,42]:

$$E(x) = A(x)\cos(k_0 x + \phi(x)),$$

$$\mathrm{d}E(x)/\mathrm{d}x = -k_0 A(x)\sin(k_0 x + \phi(x)), \qquad (21)$$

where, as in Section 5, $k_0 = \pi/a$. The above equations define the amplitude and phase functions. Their substitution into Eq. (12) gives the so-called Bogolyubov equations in standard form [41,42]:

$$\frac{\mathrm{d}\phi(x)}{\mathrm{d}x} = \frac{1}{k_0}\left[\frac{\omega^2}{c^2}\varepsilon(x) - k_0^2\right]\cos^2(k_0 x + \phi(x)),$$

$$\frac{\mathrm{d}A(x)}{\mathrm{d}x} = \frac{A(x)}{2k_0}\left[\frac{\omega^2}{c^2}\varepsilon(x) - k_0^2\right]\sin 2(k_0 x + \phi(x)). \qquad (22)$$

No approximations have been made so far. The structure of the above equation suggests that conditions $\mathrm{d}A/\mathrm{d}x \ll k_0 A$ and $\mathrm{d}\phi/\mathrm{d}x \ll k_0\phi$ can be satisfied in the vicinity of the spectral region where $(1/k_0)[\overline{\omega^2/c^2\varepsilon(x)} - k_0^2] \ll k_0$. Here, the overbar denotes an average over one period. Comparison with the analysis in Sections 3–5 shows that this condition is satisfied in the vicinity of the primary PBG. In the system of interest, for which $N \gg 1$, this observation justifies "averaging out" the fast spectral components, which is the Mitropolsky technique [42]. This averaging procedure leads to the following system of nonlinear equations for the slow-varying amplitude and phase:

$$\frac{\mathrm{d}\phi(x)}{\mathrm{d}x} = \frac{1}{2k_0}\left[\frac{\omega^2}{c^2}\varepsilon_0 - k_0^2 \right.$$
$$\left. + \frac{\omega^2}{c^2}\frac{\Delta\varepsilon/2}{1+\gamma}\left(1 + \gamma\cos\frac{2\pi}{L}x\right)\left(1 + \frac{1}{2}\cos 2\phi(x)\right)\right],$$
$$\qquad (23)$$

$$\frac{\mathrm{d}\log A(x)}{\mathrm{d}x} = \frac{1}{2k_0}\frac{\omega^2}{c^2}\frac{\Delta\varepsilon/2}{1+\gamma}\left(1 + \gamma\cos\frac{2\pi}{L}x\right)\sin 2\phi(x).$$
$$\qquad (24)$$

In deriving Eqs. (23) and (24) we have used the explicit form of $\varepsilon(x)$ given by Eq. (2).

We begin the analysis of Eqs. (23) and (24) with a discussion of the appropriate boundary conditions. In deriving these equations we have limited consideration to real-valued solutions of the original Eq. (12), which can be found only for a discrete set of frequencies. At these special frequencies, the corresponding amplitude function should reflect the periodicity of the dielectric function Eq. (2). This implies that

$$\phi(L) = \phi(0) + m\pi, \qquad (25)$$

$$\sin 2\phi(0, L/2, L) = 0. \qquad (26)$$

The first condition is obtained by requiring $\sin 2\phi(x)$ in Eq. (24) to be periodic. Symmetry of the modulation profile $A(x)$ [see Fig. 1(a)] and continuity of its derivative lead to the condition $\mathrm{d}A(x=0,L/2,L)/\mathrm{d}x=0$. This can only be satisfied by requiring Eq. (26), because other factors on the right-hand side of Eq. (24) are positive functions.

Equation (23), which determines the evolution of the phase, is self-contained. Hence, its solution together with the constraints given by Eqs. (25) and (26) is sufficient to obtain the spectrum of the system and $\phi(x)$. The amplitude is to be recovered in the second step by simple integration of Eq. (24) with the found phase $\phi(x)$.

Figure 6 shows the solutions of Eqs. (23)–(26) obtained by a fourth-order Runge–Kutta numerical method. In accord with our expectation, for each band there exist two solutions $\phi(x)$, which correspond to standing-wave band-edge modes at $K=0, \pi/L$, as seen in Figs. 6(a) and 6(e). The corresponding solutions of the amplitude equation, Fig. 6(b)–6(d), 6(f), and 6(g), agree with the envelopes extracted from direct solutions of the Helmholtz equation (Fig. 3). The eigenvalues of Eq. (23) also give the frequencies that correspond to band-edge states, and are also in excellent agreement (the observed deviation is less than 0.1%); see Fig. 3. Knowledge of the band-edge frequencies allows the determination of all parameters of the tight-binding approximation for $\omega(K)$ [Eq. (1)]. Therefore, the entire band structure in the spectral region of each of the flat bands can be obtained solely from solution of the amplitude-phase equation.

The filled circles in Figs. 6(a) and 6(e) denote the spatial position where the particular $\phi(x)$ is equal to $m\pi/2$. At these special points $\mathrm{d}A(x)/\mathrm{d}x=0$, as denoted by the vertical dashed lines in Figs. 6(b)–6(d), 6(f), and 6(g). Thus, the overall phase accumulated by $\phi(x)$ over one period is an important parameter indicative of the spatial
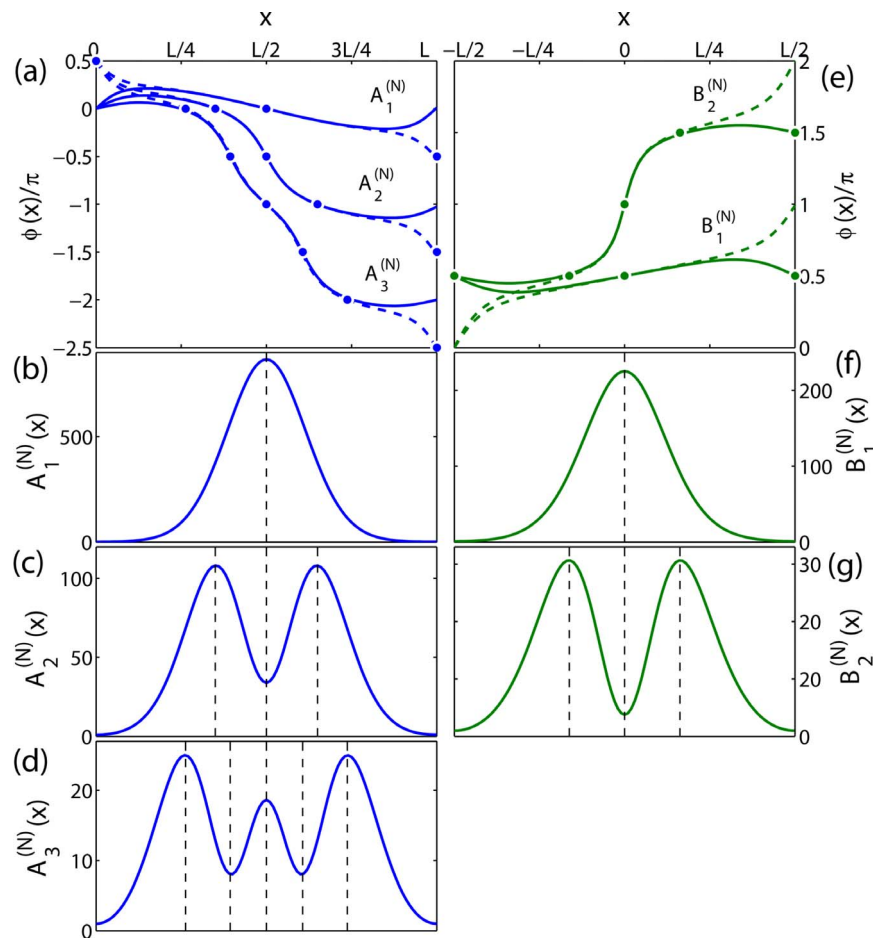
Fig. 6.   (Color online) Numerical solutions of Eqs. (23)–(26) are shown. Filled circles in panels (a) and (e) denote the spatial position where the particular $\phi(x)$ is equal to $m\pi/2$. At these special points $dA(x)/dx=0$ is denoted by the vertical dashed lines in (b)–(d), (f), and (g). $A_i^{(N)}$ and $B_i^{(N)}$ denote the low-dispersion photonic bands as defined in Section 3.

structure of the amplitude. At the band-edge frequencies of the bands $A_1^{(N)}$ and $B_1^{(N)}$ (see Section 3 for notations), the phase is a bounded function $|\phi(x)-\phi(0)| \le \pi/2$. Therefore, $x=0,L/2,L$ are the only positions where the corresponding amplitude function takes the minimum–maximum values. Thus, as seen in Figs. 6(b) and 6(f) $A(x)$ has only one "hump" for $A_1^{(N)}$ and $B_1^{(N)}$. A comparison of $\phi(x)$ computed at the $K=0$ (solid curves) and $K=\pi/L$ (dashed lines) edges of each photonic band shows (Fig. 6) that the difference occurs in the spatial regions where electromagnetic waves propagate via the "tunneling mechanism" in the language of the CROWs of Section 3. In these regions $A(x)$ is small, which explains the small spectral width of the corresponding photonic bands.

As the eigenfrequencies of the higher-order states $A_2^{(N)}, B_2^{(N)}, \ldots$ shift further away from the primary bandgap region [Fig. 1(b)], $\phi(x)$ becomes a progressively steeper function, leading to a steady increase in the number of humps in $A(x)$ [Fig. 6]. This progression accelerates the spatial dependence of the amplitude and leads to an eventual breakdown of the scale separation approximation used in the derivation of Eqs. (23) and (24). Nevertheless, such a loss of applicability occurs well outside the spectral region of interest, demonstrating the robustness of the approach developed here.

7. SUMMARY

In this work we have studied the optical properties of a dual-periodic photonic superlattice with four different theoretical methods. Although each method has its limitations, the results obtained in the framework of each model complement each other.

Numerical simulation with transfer matrices provides a direct approach for calculating the photonic band structure. This method, however, provides little physical insight into the nature of the photonic bands. In Section 3 we compared the spectrum of the infinite (periodic) crystal with the transmission spectrum of a finite system with a length equal to one period of the superstructure. We identified the individual transmission resonances with the photonic bands and found a one-to-one correspondence. Furthermore, the spatial distribution of the fields at resonance demonstrated that in the $L \gg a$ limit the envelope (amplitude) of the state changes slowly—on the scale of L.

With a method commonly employed in condensed matter physics we investigated the resonant interactions between Bloch waves when the second, longer-scale, modulation is introduced. We showed that the flattening of photonic bands is related to, but goes beyond band folding. It arises due to increased coupling between Bloch

waves with k vectors at the boundaries of the Brillouin zone. The subsequent increase of the bandgap regions "squeezes" the bands making them progressively flatter as $N = L/a$ is increased. Although, as shown in Section 4, this approach fails for very large N, it still provides insight into the origin of the anomalously small dispersion in the spectra of PhSCs.

Diffraction gratings introduced in optical fibers are often spatially modulated. Coupled-mode theory has been developed to reduce the problem to a study of the amplitudes of the forward and backward propagating waves and to avoid a direct solution of Maxwell's equations. Although the refractive index contrast induced in optical fibers is orders of magnitude smaller then in the systems we are concerned with in this work, the CMT-based approach of Section 5 provided a clear physical picture. It showed that the electromagnetic states of our optical resonators can be thought of as eigenstates of the photonic wells. This further reinforced the analogy with CROWs that we developed in Section 3.

We proceeded by noting a formal similarity between the Helmholtz equation with the considered dielectric function and the equation describing parametric resonance in oscillation theory. Adopting an amplitude-phase formalism, accompanied by a separation of scales (short a and long $L = Na$) allowed us to derive a tractable set of equations for the envelope functions. This enabled us to study physically meaningful mode profiles directly, without assuming small modulations of the refractive index.

We find that the dual-periodic photonic lattice is a promising system for studying slow-light phenomena. It can be viewed as an array of evanescently coupled optical cavities. The cavities are formed due to the presence of a second, long-range modulation, which creates alternating spatial regions of allowed and forbidden propagation. Thus, analogies with multiple-quantum-well and coupled resonant optical arrays (CROWs) are appropriate. Unlike other CROW implementations, the structures studied can be produced with a holography-based approach, which enables fabrication of arrays with a large number of identical resonators. The latter is a crucial condition from an experimental point of view, and should ensure that the resonances of the individual cavities couple to form flat photonic bands.

ACKNOWLEDGMENTS

REFERENCES

1. C. M. Soukoulis, ed., *Photonic Band Gap Materials* (Kluwer, Dordrecht, 1996).
2. P. W. Milonni, *Fast Light, Slow Light and Left-Handed Light* (Institute of Physics, 2005).
3. S. Nojima, "Enhancement of optical gain in two-dimensional photonic crystals with active lattice points," Jpn. J. Appl. Phys., Part 2 **37**, L565–L567 (1998).
4. K. Sakoda, "Enhanced light amplification due to group-velocity anomaly peculiar to two- and three-dimensional photonic crystals," Opt. Express **4**, 167–176 (1999).
5. N. Susa, "Threshold gain and gain-enhancement due to distributed-feedback in two-dimensional photonic-crystal lasers," J. Appl. Phys. **89**, 815–823 (2001).
6. Yu. A. Vlasov, M. O'Boyle, H. F. Hamann, and S. J. McNab, "Active control of slow light on a chip with photonic crystal waveguides," Nature **438**, 65–69 (2005).
7. J. K. S. Poon, J. Scheuer, Y. Xu, and A. Yariv, "Designing coupled-resonator optical waveguide delay lines," J. Opt. Soc. Am. B **21**, 1665–1673 (2004).
8. J. Scheuer, G. Paloczi, J. Poon, and A. Yariv, "Toward the slowing and storage of light," Opt. Photonics News **16**, 36–40 (2005).
9. Y. Xu, R. K. Lee, and A. Yariv, "Propagation and second-harmonic generation of electromagnetic waves in a coupled-resonator optical waveguide," J. Opt. Soc. Am. B **17**, 387–400 (2000).
10. M. Soljacic, S. G. Johnson, S. Fan, M. Ibanescu, E. Ippen, and J. D. Joannopoulos, "Photonic-crystal slow-light enhancement of nonlinear phase sensitivity," J. Opt. Soc. Am. B **19**, 2052–2059 (2002).
11. R. S. Jacobsen, K. N. Andersen, P. I. Borel, J. Fage-Pedersen, L. H. Frandsen, O. Hansen, M. Kristensen, A. V. Lavrinenko, G. Moulin, H. Ou, C. Peucheret, B. Zsigri and A. Bjarklev, "Strained silicon as a new electro-optic material," Nature **441**, 199–202 (2006).
12. E. Yablonovitch, "Inhibited spontaneous emission in solid-state physics and electronics," Phys. Rev. Lett. **58**, 2059–2062 (1987).
13. J. F. Galisteo-López and C. López, "High-energy optical response of artificial opals," Phys. Rev. B **70**, 035108 (2004).
14. M. Scharrer, A. Yamilov, X. Wu, H. Cao, and R. P. H. Chang, "Ultraviolet lasing in high-order bands of three-dimensional ZnO photonic crystals," Appl. Phys. Lett. **88**, 201103 (2006).
15. L. A. Dorado, R. A. Depine, and H. Miguez, "Effect of extinction on the high-energy optical response of photonic crystals," Phys. Rev. B **75**, 241101 (2007).
16. N. Stefanou and A. Modinos, "Impurity bands in photonic insulators," Phys. Rev. B **57**, 12127–12133 (1998).
17. A. Yariv, Y. Xu, R. K. Lee, and A. Scherer, "Coupled-resonator optical waveguide: a proposal and analysis," Opt. Lett. **24**, 711–713 (1999).
18. J. K. S. Poon, L. Zhu, G. A. DeRose, and A. Yariv, "Polymer microring coupled-resonator optical waveguides," J. Lightwave Technol. **24**, 1843–1849 (2006).
19. H. Altug and J. Vuckovic, "Experimental demonstration of the slow group velocity of light in two-dimensional coupled photonic crystal microcavity arrays," Appl. Phys. Lett. **86**, 111102 (2005).
20. M. Bayindir, S. Tanriseven, and E. Ozbay, "Propagation of light through localized coupled-cavity modes in one-dimensional photonic band-gap structures," Appl. Phys. A **72**, 117–119 (2001).
21. M. Bayindir, C. Kural, and E. Ozbay, "Coupled optical microcavities in one-dimensional photonic bandgap structures," J. Opt. A, Pure Appl. Opt. **3**, S184–S189 (2001).
22. R. Shimada, T. Koda, T. Ueta, and K. Ohtaka, "Strong localization of Bloch photons in dual-periodic dielectric multilayer structures," J. Appl. Phys. **90**, 3905–3909 (2001).
23. H. Kitahara, T. Kawaguchi, J. Miyashita, R. Shimada, and M. W. Takeda, "Strongly localized singular bloch modes created in dual-periodic microstrip lines," J. Phys. Soc. Jpn. **73**, 296–299 (2004).
24. R. Shimada, T. Koda, T. Ueta, and K. Ohtaka, "Energy spectra in dual-periodic multilayer structures," J. Phys. Soc. Jpn. **67**, 3414–3419 (1998).

25. Z.-W. Liu, Y. Du, J. Liao, S.-N. Zhu, Y.-Y. Zhu, Y.-Q. Qin, H.-T. Wang, J.-L. He, C. Zhang, and N.-B. Ming, "Engineering of a dual-periodic optical superlattice used in a coupled optical parametric interaction," J. Opt. Soc. Am. B **19**, 1676–1684 (2002)

26. J. E. Sipe, L. Poladian, and C. Martin de Sterke, "Propagation through noniniform grating structures," J. Opt. Soc. Am. A **11**, 1307–1320 (1994).

27. J. M. Benedickson, J. P. Dowling, and M. Scalora, "Analytic expressions for the electromagnetic mode density in finite, one-dimensional, photonic band-gap structures," Phys. Rev. E **53**, 4107–4121 (1996).

28. D. Janner, G. Galzerano, G. Della Valle, P. Laporta, S. Longhi, and M. Belmonte, "Slow light in periodic superstructure Bragg grating," Phys. Rev. E **72**, 056605 (2005).

29. K. Yagasaki, I. M. Merhasin, B. A. Malomed, T. Wagenknecht, and A. R. Champneys, "Gap solitons in Bragg gratings with a harmonic superlattice," Europhys. Lett. **74**, 1006–1012 (2006).

30. A. Yamilov and M. Bertino, "Disorder-immune coupled resonator optical waveguide," Opt. Lett. **32**, 283–285 (2007).

31. M. F. Bertino, R. R. Gadipalli, J. G. Story, C. G. Williams, G. Zhang, C. Sotiriou-Leventis, A. T. Tokuhiro, S. Guha, and N. Leventis, "Laser writing of semiconductor nanoparticles and quantum dots," Appl. Phys. Lett. **85**, 6007–6009 (2004).

32. M. F. Bertino, R. R. Gadipalli, L. A. Martin, L. E. Rich, A. Yamilov, B. R. Heckman, N. Leventis, S. Guha, J. Katsoudas, R. Divan, and D. C. Mancini, "Quantum dots by ultraviolet and X-ray lithography," Nanotechnology **18**, 315603 (2007).

33. D. Marcuse, *Theory of Dielectric Optical Waveguides*, 2nd ed. (Academic, 1991).

34. J. W. Fleischer, T. Carmon, M. Segev, N. K. Efremidis, and D. N. Christodoulides, "Observation of discrete solitons in optically induced real time waveguide arrays," Phys. Rev. Lett. **90**, 023902 (2003).

35. D. Neshev, E. Ostrovskaya, Y. Kivshar, and W. Krolikovwski, "Spatial solitons in optically induced gratings," Opt. Lett. **28**, 710–712 (2003).

36. N. K. Efremidis, S. Sears, D. N. Christodoulides, J. W. Fleischer, and M. Segev, "Discrete solitons in photorefractive optically induced photonic lattices," Phys. Rev. E **66**, 046602 (2002).

37. P. Yeh, *Optical Waves in Layered Media* (Wiley, 2005).

38. I. M. Lifshitz, S. A. Gredeskul, and L. A. Pastur, *Introduction to the Theory of Disordered Systems* (Wiley, 1988).

39. N. W. Ashcroft and N. D. Mermin, *Solid State Physics* (Brooks Cole, 1976).

40. C. M. de Sterke, "Superstructure gratings in the tight-binding approximation," Phys. Rev. E **57**, 3502–3509 (1998).

41. P. S. Landa, *Regular and Chaotic Oscillations* (Springer, 2001).

42. N. N. Bogolyubov and Yu. A. Mitropolsky, *Asymptotic Methods in Theory of Nonlinear Oscillations* (Nauka, 1974) (in Russian).